RSC Advances

PAPER

View Article Online
View Journal | View Issue

Cite this: *RSC Adv.*, 2017, **7**, 24097

Facile synthesis of g-C_3N_4 nanosheets loaded with WO_3 nanoparticles with enhanced photocatalytic performance under visible light irradiation†

Jie Meng, Jingyuan Pei, Zefang He, Shiyan Wu, Qingyun Lin, Xiao Wei,* Jixue Li and Ze Zhang

Received 24th February 2017
Accepted 25th April 2017

DOI: 10.1039/c7ra02297b

rsc.li/rsc-advances

Graphitic carbon nitride (g-C_3N_4) nanosheets loaded with WO_3 nanoparticles were prepared *via* heat treatment of g-C_3N_4 together with WO_x-EDA nanobelts. The thermal treatment temperature and WO_x-EDA precursor play the key role in enhancing the interaction between WO_3 nanoparticles and g-C_3N_4 nanosheets, because the temperature of thermal decomposition of WO_x-EDA (~400 °C) is close to the thermal exfoliation temperature of g-C_3N_4. The structure evolution and promotion effect of the nanocomposites in photocatalytic performance were well studied. It is found that WO_3 nanoparticles uniformly dispersed on the surface of the g-C_3N_4 nanosheets, and the close integration of WO_3 and g-C_3N_4 lead to the high photocatalytic activity in the degradation of RhB under visible light irradiation. Meanwhile, a larger specific area and increase of visible light absorption are also of benefit to speed up the degradation of organic dye. Also, the mechanism of the photocatalytic reaction and its reutilization properties were investigated.

Introduction

Photocatalysts have been receiving much attention as a promising material in recent years due to their applications in alleviating global environmental pollution and the energy crisis, such as waste pollutant degradation,[1,2] water splitting[3] and CO_2 reduction.[4] However, there are some major challenges that hamper the requirements of their practical applications, for instance, a high recombination rate of photo-excited charge carriers, low solar energy conversion efficiency resulting from a wide band gap, and other restrictions.[5,6] Accordingly, it is essential to develop a high performance photocatalyst that could not only enhance the separation and transportation efficiency of electron–hole pairs but also improve the light absorption properties under solar radiation.

Graphitic carbon nitride (g-C_3N_4), a great potential material for photocatalytic reaction first reported by Wang *et al.* in early 2009,[7] has received intensive attention on account of its unique electronic and optical properties, such as visible light response, good reduction ability, easy synthesis, and high stabilities. What's more, the band gap of g-C_3N_4 is around 2.7 eV, which could absorb visible light up to 460 nm correspondingly.[8,9] The conduction band edge potential of g-C_3N_4 is more negative (about −1.12 eV *vs.* NHE), therefore, photo-induced electrons would have high reduction capacity.[10,11] Nevertheless, it has been concluded that the low photocatalytic activities of g-C_3N_4 are mainly attributed to high recombination of photo-generated charge carriers and low specific surface area.[12–14] Many efforts have been made to overcome these bottlenecks. It was reported that ultrasonic vibration,[15] thermal exfoliation[16] and hydrothermal treatment[17] could be used to change the BET surface area. Meanwhile, doping,[18] noble metal loading[19] and coupling with other semiconductors[8] are also effective methods to achieve the separation of carriers and then further increase the photocatalytic performance under visible light illumination. Among all the strategies, coupling with other semiconductors is an efficient attempt to solve above two questions due to the suitable band position and enhanced hole–electron pairs transfer between the two semiconductors by appropriate combination style. Especially, g-C_3N_4 nanosheets which show distinct physical and chemical features with larger specific area and outstanding electronic mobility,[20,21] are considered to be an appropriate candidate to couple with other semiconductors to form high-performance photocatalysts. As a matter of fact, many progresses have been made on g-C_3N_4 nanosheets based composites,[22] such as TiO_2/g-C_3N_4,[23] ZnO/g-C_3N_4,[24] Bi_2WO_6/g-C_3N_4,[25] MoS_2/g-C_3N_4,[26] *etc.* These composite systems have deservedly achieved enhanced photocatalytic performance which is generally ascribed to the improved reaction sites, charge separation and migration processes. Nevertheless, it is necessary for a practical photocatalyst to be provided with

Center of Electron Microscopy, State Key Laboratory of Silicon Materials, School of Materials Science and Engineering, Zhejiang University, Hangzhou, 310027, P. R. China. E-mail: mseweixiao@zju.edu.cn; Fax: +86 571 87952797; Tel: +86 571 87952797

† Electronic supplementary information (ESI) available. See DOI: 10.1039/c7ra02297b

stable crystal structure, narrow band gap, low material cost, and easy preparation. So there is still a long way to seek a proper material coupling with g-C_3N_4 nanosheets to form highly active composite photocatalysts.

Alternatively, tungsten(VI) oxide (WO_3) which is deemed as a promising material of photocatalysts[27] with a narrow band gap of about 2.7 eV, is a potential candidate to form composites with g-C_3N_4 nanosheets to get excellent photocatalytic performance. Meanwhile, its stable crystal structure, resistance to photo-corrosion, and inexpensiveness are all important issues for the practical application.[28] The VB edge potential of WO_3 is more positive, implying that it has a better oxidation capability in photocatalytic activities. However, the CB position of WO_3 limits its photocatalytic reaction under visible light illumination since this CB level is not beneficial to the single-electron reaction of O_2.[29,30] It could decrease the recombination of hole–electron pairs and make up the defects of the conduction band by synergistic effect of two semiconductors when WO_3 coupling with g-C_3N_4.[30] Therefore, WO_3 is a proper candidate to form composites with g-C_3N_4 to achieve excellent photocatalytic performance under visible light irradiation. However, for photocatalytic composites, the separation efficiency of photo-induced carriers is not only related to appropriate electronic structures, but most importantly determined by effective combination with better contact, that is still a challenge for most semiconductor composites. Many attempts have been applied to form WO_3/g-C_3N_4 composites to achieve the above goals, but there are no reports about using the WO_x-EDA nanobelts, as the precursor of WO_3 to synthesize WO_3/g-C_3N_4 composites with a suitable combination method which could not only enlarge the specific surface area but also restrain the recombination of photo-excited carriers.[29–33] The WO_x-EDA nanobelts was synthesized by solvothermally treating WO_3 in ethanediamine (EDA) following a so-called solvent-coordination molecular template (SCMT) mechanism.[34]

In this paper, we prepared the WO_3/g-C_3N_4 composites through heat treatment of WO_x-EDA and g-C_3N_4. Since the decomposition temperature (around 400 °C) of WO_x-EDA is close to thermal exfoliation temperature of g-C_3N_4, both of two reaction processes conduct simultaneous, which was found to facilitate WO_3 nanoparticles to uniformly disperse on g-C_3N_4 nanosheets. The photocatalytic performance of the WO_3/g-C_3N_4 composites was evaluated by the degradation of Rhodamine B under visible light illumination. The decrease of recombination of photo-generated hole–electron pairs evaluated by photoluminescence (PL) spectra, larger specific surface area calculated by BET method and enhanced visible light absorption characterized by diffuse reflectance spectrum (DRS) are main reasons to increase photocatalytic activity. Based on the systematically characterizations of the photocatalysts, a possible mechanism for the enhanced photocatalytic performance of WO_3/g-C_3N_4 composites is proposed.

Experimental section

Materials and synthesis

All of the chemical reagents used in this experiment were of analytical stage without further purification.

Pristine g-C_3N_4 synthesis. Pristine g-C_3N_4 was prepared by directly heating melamine in muffle furnace.[35] In a typical procedure, melamine powder was put into alumina crucible with a cover, then heated to 550 °C for 4 h at a heating rate of 3.5 °C min^{-1}; after cooling to room temperature in the way of furnace cooling, the yellow powder was ground and collected for subsequent use.

WO_x-EDA synthesis. The WO_x-EDA was synthesized by solvothermal treatment of m-WO_3 (monoclinic WO_3), and m-WO_3 was prepared by hydrothermal route. Firstly, 10 mmol $Na_2WO_4 \cdot 2H_2O$ was dissolved in distilled water (40 mL), then 5 mL of HNO_3 was added into aqueous solution under stirring at room temperature. After stirring for about 1 h, the mixture was transferred into a 50 mL Teflon-lined stainless-steel autoclave, heated to 200 °C for 48 h and then cooled to room temperature naturally. The yellow product, named m-WO_3, was washed, dried, ground and collected for next use. Secondly, WO_x-EDA was prepared according to previous report similarly.[34] Typically, 1 g of as-prepared m-WO_3 powder and 40 mL of ethanediamine (EDA) were mixed under stirring for 60 min. The mixture was heated to 200 °C for 12 h by solvothermal treatment. After cooling to room temperature, the product was collected after washed, dried and ground for subsequent use, namely WO_x-EDA (Fig. S1†).

WO_3/g-C_3N_4 composites synthesis. Typically, 0.4 g WO_x-EDA and 1 g pristine g-C_3N_4 were mixed in ethanol solution under ultrasonication for 1 h, and then dried at 80 °C for about 12 h (Fig. S2†). The obtained mixture was annealed to 400 °C for 2 h, and the final sample is called WECN40. According to different mass ratio between WO_x-EDA and g-C_3N_4, the samples are named CN or g-C_3N_4, WECN20, WECN40, WECN60, WECN80 and WO_3 (Scheme 1). All above six samples were prepared using the same treating process as same as WECN40.

Characterization

The crystalline phases of the as-synthesized samples were characterized by X-ray diffraction (XRD, PANalytical X'Pert PRO) with Cu Kα radiation with 2θ from 10–80°. The morphology and composition of the as-obtained samples were investigated by field emission scanning electron microscopy (SEM, Hitachi SU-70) and transmission electron microscopy (TEM, FEI Tecnai G^2 F20 S-TWIN) equipped with an energy dispersive X-ray spectrometer (EDX). Specific surface area (S_{BET}) was determined with a surface area analyser (Quantachrome AUTOSORB-IQ2-MP) by the BET method. Diffuse reflectance spectra (DRS) was measured by a UV-vis spectrophotometer (Persee TU-1900)

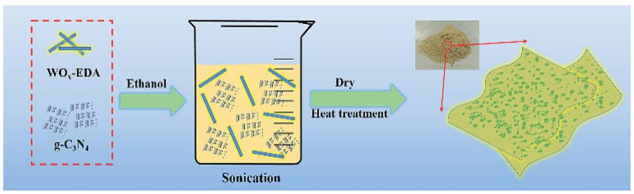

Scheme 1 Schematic presentation of the synthesis process of WO_3/g-C_3N_4 composites.

equipped with an integrating sphere unit using $BaSO_4$ as the reflectance standard. Photoluminescence (PL) spectra was obtained by fluorescence spectrometer (Edinburgh instruments FLS920). Fourier transform infrared (FTIR) spectra of samples was recorded using a Nicolet Avatar-370 spectrometer at room temperature. The surface electronic states of the samples were measured by X-ray photoelectron spectroscopy (XPS, Escalab 250Xi). The concentration of phenol was characterized by liquid chromatograph (C18-ODS column).

Photocatalytic measurement

The photocatalytic performances of the WO_3/CN samples were characterization by the degradation of Rhodamine B (RhB) under visible light. A 300 W xenon lamp acts as a visible light source equipped with a UV cutoff filter ($\lambda > 420$ nm) during the experiment. For photocatalytic test, 0.05 g of the photocatalyst was dissolved in 100 mL of 10 mg L^{-1} RhB solution in a glass beaker. Before irradiation, the solution was magnetically stirred in the dark for 30 minutes to achieve adsorption–desorption equilibrium between photocatalyst and dye. After the illumination, 5 mL of solution was taken from the reaction suspension and centrifuged to remove the particles every time before measuring the absorption spectra. The UV-vis spectrophotometer (Persee TU-1900) was used to study the concentration of RhB in solution. The characteristic absorption peak of RhB at 554 nm was used to determine the extent of its degradation.

Electrochemical analysis

Electrochemical measurements were conducted on a CHI 760 electrochemical workstation in a standard three-electrode cell, using a Pt plate as counter electrode and an Ag/AgCl electrode as reference electrode and photocatalyst-coated FTO conductive glass slides (*ca.* 2 cm^2) as working electrode, respectively. Na_2SO_4 aqueous solution was selected as the electrolyte. The working electrode was prepared by follow deposition method: 20 mg sample powder was mixed in 40 mL PEG10000 solution, sonicated for 30 min and as-prepared solution was drop onto FTO. Then, parallel FTO glasses were placed in the drying oven for at 100 °C for 6 h. Finally, as-prepared FTO glasses with sample film were annealed at 300 °C for 3 h in muffle furnace. The bias voltage was set at −0.5 V *vs.* Ag/AgCl. 300 W Xe lamp with a UV filter ($\lambda > 420$ nm) served as light source in the photocurrent tests obtained at 0.5 V *vs.* Ag/AgCl.

Results and discussion

Characterization of WO_3/g-C_3N_4 composites

Fig. 1 shows the XRD patterns of g-C_3N_4, WO_3 and serials WO_3/g-C_3N_4 composite photocatalysts. It is observed that two diffraction peaks areas around 27.7° and 12.9° for g-C_3N_4 (JCPDS 87-1526), are corresponding to the (002) and (100) diffraction planes, respectively. According to the reported results,[36] the stronger peak at 27.7° corresponds to the interlayer stacking of the aromatic systems with the interlayer distance of 0.322 nm. The weaker one at 12.9° which attributes to a distance around $d = 0.686$ nm is related to in-plane tris-*s*-triazine structural packing. For WO_3, it can be index to the monoclinic structure (JCPDS card no. 83-0950 with lattice parameters of $a = 7.301$ Å, $b = 7.539$ Å, $c = 7.690$ Å and $\alpha = \gamma = 90°$, $\beta = 90.892°$) and the main diffraction peaks at 23.3°, 23.7°, 24.5°, 26.7°, 28.8°, 34.3°, 41.7°, 50.0°, and 55.94° are corresponding to (002), (020), (200), (120), (112), (202), (222), (400), and (420) planes, respectively. For WO_3/g-C_3N_4 composites, the XRD patterns reveal a coexistence of WO_3 and g-C_3N_4. The intensity of characteristic (002) peak assigned to g-C_3N_4 becomes weaker with the increasing WO_3 content in the composites gradually. The (100) peak ascribed to g-C_3N_4 is not observed in the composites which may be due to the relative low intensity compared to WO_3. The main peak changes slightly compared to original 27.7° for g-C_3N_4 resulted from the introduction of WO_3 indicate that a small shift of interlayers for the interaction between WO_3 and g-C_3N_4.

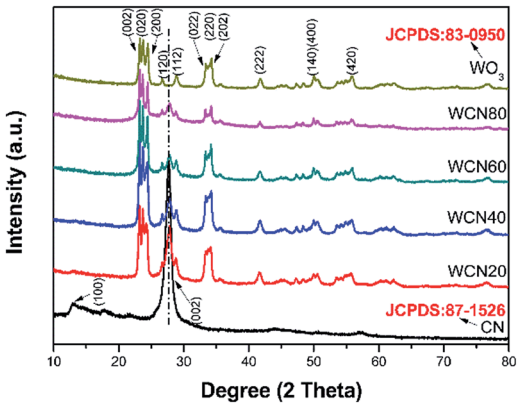

Fig. 1 XRD patterns of g-C_3N_4, WO_3 and WO_3/g-C_3N_4 composite photocatalysts.

The morphologies and microstructures of the as-obtained samples are shown in Fig. 2 and S3.† As seen in Fig. 2(a), g-C_3N_4 displays a sheet-like structure with different thickness through high or low contrast in the picture. This microstructure

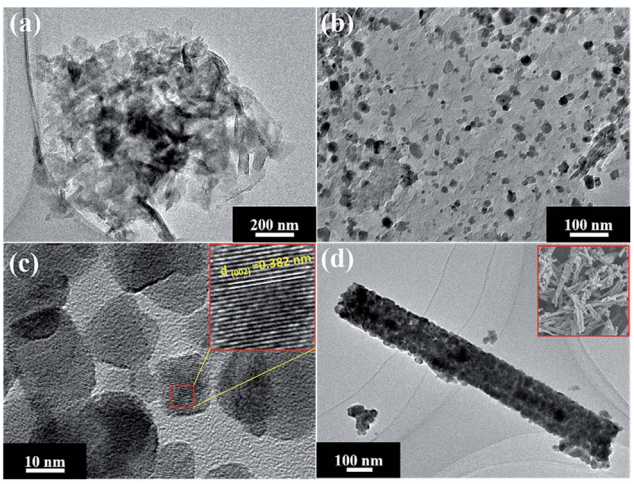

Fig. 2 TEM images of (a) CN; (b) WECN40; (c) high resolution TEM of WECN40; (d) WO_3 (the SEM images could be observed by the inset).

of g-C_3N_4 is consistent with our assumption after the process of ultrasonic and thermal exfoliation. As can be seen in Fig. 2(b), WO_3 particles are deposited on the surface of g-C_3N_4 in the WO_3/g-C_3N_4 composite (WECN40) morphology. The crystal phase of particles is attributed to monoclinic WO_3 which could be demonstrated by high resolution transmission electron microscopy (HRTEM) in Fig. 2(c). The fringes of particles match the crystallographic plane of WO_3 described in Fig. 2(c) and the interfaces in WO_3/g-C_3N_4 composites are thought to be beneficial to suppress the recombination of hole and election under photo-excited environment. The Fig. 2(d) presents the morphology of pure WO_3 nanobelts prepared without the g-C_3N_4. From the SEM images, it is clearly found that WO_3 nanobelts are mainly composed of nanoparticles due to the thermal decomposition of EDA.[37] These results are according with the XRD results. As shown in Fig. S4,† the peaks of EDS spectrum for WO_3/g-C_3N_4 composites are ascribed to C, N, O and W, the presence of Cu and partly high intensity of C are due to the influence of the micro grid, implying that the composites are composed of WO_3 and g-C_3N_4 without any kind of impurity. The FT-IR spectra of g-C_3N_4, WO_3 and WO_3/g-C_3N_4 composite (WECN40) are presented in Fig. 3. For pure g-C_3N_4, several strong bands in the 1000–1650 cm^{-1} region and the peak at 810 cm^{-1} were observed, which belong to the *s*-triazine ring modes.[38,39] The absorption peaks at 1638 cm^{-1} and 1238 cm^{-1} are attributed to the C=N and C–N stretching modes respectively.[40–43] The sharp peak at 1638 cm^{-1} is an indication of good crystallinity of g-C_3N_4 crystals. Also, broad bands of stretching and deformation modes of the NH_2 (as well as an overlapping band of O–H stretching possibly) groups at 3414 cm^{-1}.[44] The broad absorption peak at 817 cm^{-1} is assigned to O–W–O stretching vibrations for WO_3. Obviously, the characteristic peaks of g-C_3N_4 between 800 and 1600 cm^{-1} weaken to some extent when combined with WO_3. The peak at 3414 cm^{-1} for all samples is attributed to O–H stretching vibration and the bending vibration of adsorbed water molecules is located at 1620 cm^{-1} for samples.[45]

XPS spectra are shown in Fig. 4 to analyse the surface chemical composition and chemical state. It is observed that as-synthesized WO_3/g-C_3N_3 composites are primarily composed of the elements like W, O, C and N from the XPS survey spectrum in Fig. 4(a). It is clearly seen that g-C_3N_4 and WO_3 are coexist in composite and slight shift of peaks indicates the interaction between g-C_3N_4 and WO_3 is exist indeed. The W4f spectrum (Fig. 4(b)) centred at 35.0 eV is ascribed to $4f_{7/2}$ and the other peak at 37.1 eV is ascribed to $4f_{5/2}$, which indicate that they are the typical valence state peaks of W^{6+}.[46–48] Two peaks (Fig. 4(c)) are showed at about 529.4 eV and 531.8 eV for O1s XPS spectra, which could be associated with W–O–W and W–O–H, respectively.[49] The C1s peaks (Fig. 4(d)) could be separated into three characterization parts: the peak located at 287.3 eV is typically related to the sp^2-bonded N=C–N, the peak centred at 285.9 eV is attributed to the C–O species on the g-C_3N_4 surface and the peak at 284.6 eV can be assigned to C–C may due to the surface adventitious carbon or defect in the g-C_3N_4.[50,51] Additionally, the N1s peaks (Fig. 4(e)) can be deconvoluted into three peaks at 398.4 eV, 399.7 eV, and 400.8 eV which refer to triazine rings (C=N–C), tertiary nitrogen (N–$(C)_3$), and amino functions (C–N–H).[52] Fig. 4(f) shows valence band spectra of samples and valence band potentials of g-C_3N_4 and WO_3 are 1.62 and 2.70 eV respectively. The changes of electronic structure for WO_3/g-C_3N_4 (WECN40) indicate that the existence of interaction between g-C_3N_4 and WO_3 compared to pure WO_3 and g-C_3N_4 (Fig. S5 and S6†) and that would be beneficial to photocatalytic performance.

As can be seen in Fig. 5(a), the UV-vis diffuse reflectance spectra of g-C_3N_4, WO_3, WO_3/g-C_3N_4 composites are exhibited. For WO_3/g-C_3N_4 composites, they are red-shifted in the region

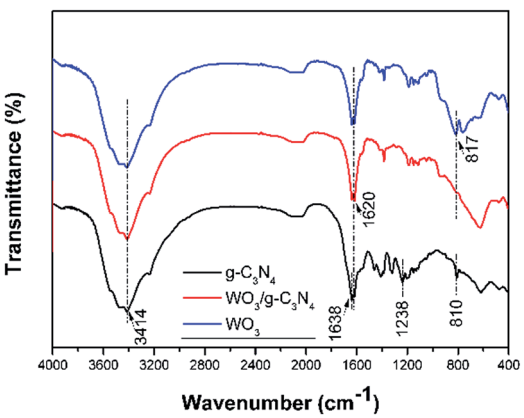

Fig. 3 FT-IR spectra of g-C_3N_4, WO_3 and WO_3/g-C_3N_4 composite (WECN40).

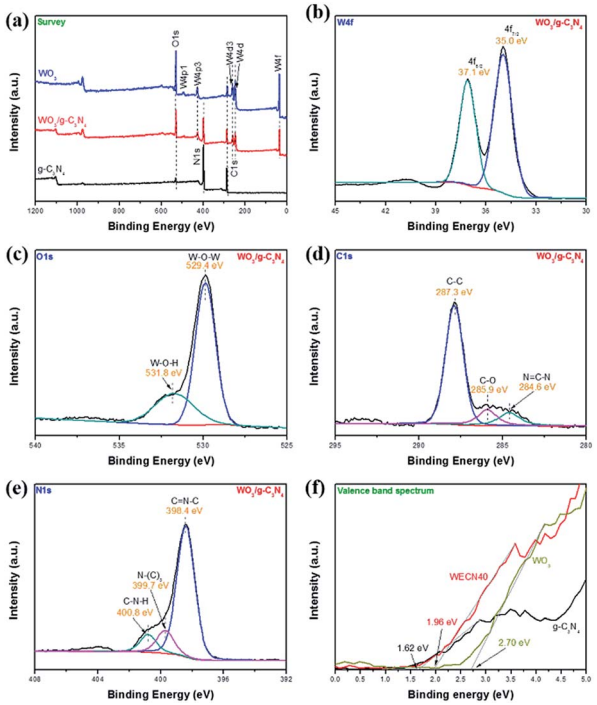

Fig. 4 (a) XPS survey spectra of g-C_3N_4, WO_3 and WO_3/g-C_3N_4 composite (WECN40); high revolution XPS spectra of (b) W4f, (c) O1s, (d) C1s, (e) N1s; (f) valence band spectra of g-C_3N_4 and WO_3.

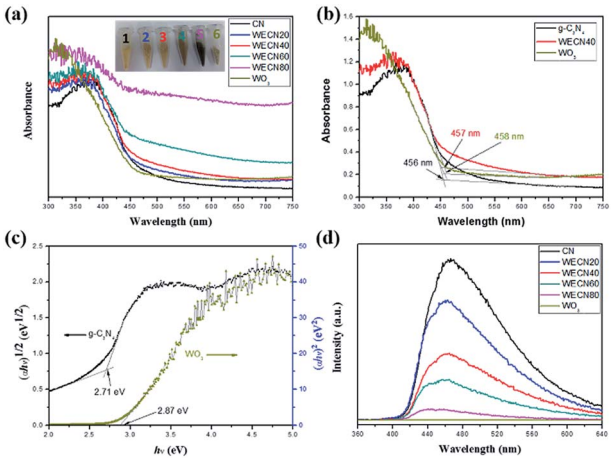

Fig. 5 (a) UV-vis diffuse reflectance spectra of g-C_3N_4, WO_3 and WO_3/g-C_3N_4 composites (the different number colors marked in samples are consistent with the nomination of samples); (b) the band gap determination of g-C_3N_4, WO_3 and WECN40 by Tanc's approach; (c) the optical transition type determination of g-C_3N_4 and WO_3; (d) PL spectra of g-C_3N_4, WO_3 and WO_3/g-C_3N_4 composites.

of 300–750 nm and the absorption ability increases with the increasing amount of WO_3, which is consistent with gradually darken colour of samples (inset of Fig. 5(a)). It is observed that the composite sample WECN40 shows stronger absorption in the visible region at wavelengths more than around 400 nm compared with g-C_3N_4 and WO_3. The band gap of samples can be estimated by the following equation:

$$(ah\nu)^{n/2} = A(h\nu - E_g)$$

where a, h, ν, A, E_g are absorption coefficient, Plank constant, light frequency, proportionality constant and band gap, respectively. The factor n is related to the optical transition of a semiconductor that $n = 1$ for direct transition and $n = 4$ for indirect transition. The values of $n = 1$ and 4 are corresponding to g-C_3N_4 and WO_3 respectively.[53,54] From Fig. 5(b), the values of the absorption bands located at 456 and 458 nm are ascribed to g-C_3N_4 and WO_3, exhibiting good absorption ability in the visible region, and the corresponding band gaps are 2.71 and 2.87 eV respectively (Fig. 5(c)). Meanwhile, the value at 457 nm of the WO_3/g-C_3N_4 composite for WECN40 is between 456 and 458 nm and red shift which occurs among all WO_3/g-C_3N_4 composites in absorption curves may be attributed to the interaction between g-C_3N_4 and WO_3 shown in Fig. 5(a and b). The positions of valence band (VB) and conduction band (CB) could be estimated by the following equation:

$$E_{VB} = X - E^c + 0.5E_g$$

$$E_{CB} = E_{VB} - E_g$$

In this equation, E_{VB}, X, E^c, E_{CB}, and E_g are defined as the VB edge potential, the electronegativity of the semiconductor, the energy of free electrons on the hydrogen scale (around 4.5 eV), the CB edge potential and the band gap energy of the semiconductor respectively.[55] The valence band edge potential of g-C_3N_4 and WO_3 are 1.62 and 2.70 eV respectively from above XPS analysis (Fig. 5(f)). And the conduction band potentials of g-C_3N_4 and WO_3 are calculated to be −1.09 eV and −0.17 eV, respectively.

Fig. 5(d) shows the PL spectra of g-C_3N_4, WO_3 and WO_3/g-C_3N_4 composites under the excitation wavelength of 325 nm. For g-C_3N_4, a strong emission band centred at about 465 nm could be attributed to the band–band PL phenomenon of photo-excited electron–hole.[56] While a weak emission peak of WO_3 could be related to localized state in the band gap with the existence of defects or oxygen vacancies.[57] It is clear that the peak intensities for WO_3/g-C_3N_4 composites decrease with the increase of WO_3. This means that an increasing number of charge carriers take part in photocatalytic reactions since the lower PL intensities implied a slower recombination rate of the photo-generated electron–hole pairs. Meanwhile, this result also indicates that the interfaces between g-C_3N_4 and WO_3 do promote the separation and migration of photo-induced charge carriers.

As shown in Fig. 6(a), the BET surface area of samples is determined by nitrogen adsorption and desorption isotherms. The S_{BET} of WECN40 composites (Table S1†) increased by 1.81 and 1.96 times compared to pure g-C_3N_4 and WO_3 photocatalysts, indicating that the interaction between g-C_3N_4 nanosheets and WO_3 nanoparticles (about 19.8 nm calculated by Scherrer equation) enlarges the BET surface area and corresponding composite materials provide more reaction sites for photodegradation. From Fig. 6(b) and Table S1,† average pore diameters of g-C_3N_4, WO_3 and WO_3/g-C_3N_4 composite (WECN40) are distributed at about 51.796, 2.105, 19.844 nm, which corresponds to the pore volume of 0.166, 0.167, 0.046 cm g^{-1}. It means that WECN40 is a photocatalyst with smaller pore diameter and larger pore volume. The pore volume of WO_3/g-C_3N_4 composite is almost the same as pure g-C_3N_4 but it has smaller pore diameter, which can be relate to the presence of WO_3 particles dispersing on g-C_3N_4 nanosheets.

Photocatalytic performance and stability of the WO_3/g-C_3N_4 composites

The photocatalytic performance of samples was investigated by the degradation of RhB under visible light illumination. As depicted in Fig. 7(a), for WO_3/g-C_3N_4 composite (WECN40), the absorption peak of the RhB solution decreased with the increase of time which indicates the photodegradation of RhB

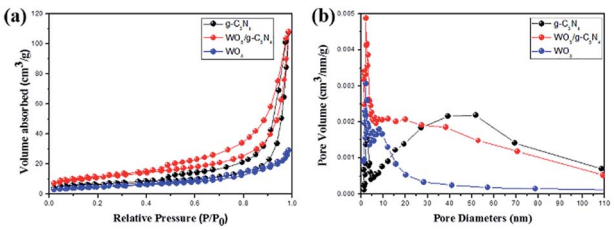

Fig. 6 (a) N_2 adsorption–desorption isotherm and (b) pore size distribution curves of g-C_3N_4, WO_3 and WO_3/g-C_3N_4 composite (WECN40).

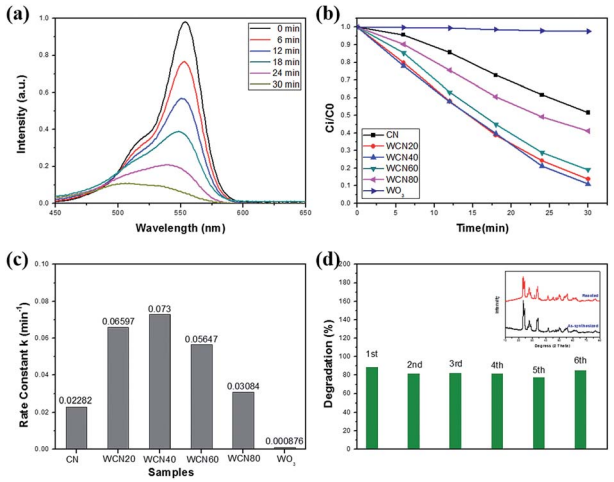

Fig. 7 (a) Photodegradation of RhB with WECN40; (b) C_i/C_0 of all the samples; (c) rate constants k values of all the photocatalysts; (d) recyclability of WECN40.

under visible light. And the blue shift from 554 to 503 nm for the wavelength of maximum characteristic peak could be attributed to *N*-deethylation mechanism in photocatalytic reaction.[58] The (C_i/C_0) of all the samples are shown in Fig. 7(b), it is obvious that WO_3/g-C_3N_4 composites display much higher photocatalytic capability compared with pure g-C_3N_4 and WO_3. The photocatalyst of WECN40 exhibits best degradation rate of contamination. In order to further estimate the photocatalytic reactions of pollutants in aqueous solutions, the first order equation of the Langmuir–Hinshelwood model is used to as follows:[59]

$$\ln(C_i/C_0) = kt$$

where C_i is the concentration of the organic dye at time t and C_0 is the initial concentration of dye in solution. Fig. 7(c) depicts the Plot of $\ln(C_i/C_0)$ *versus* irradiation time t for the catalysts. The rate constant k of all WO_3/g-C_3N_4 composites show higher photocatalytic performance than pure g-C_3N_4 and WO_3. Furthermore, the highest k value, corresponding to the WECN40 sample ($k = 0.073$ min^{-1}), is 3.2 and 83.3 times as high as that of g-C_3N_4 ($k = 0.0228$ min^{-1}) and WO_3 ($k = 0.00088$ min^{-1}), respectively. The improved photocatalytic performance could be ascribed to a synergistic effect of g-C_3N_4 and WO_3 from their effective coupling which gives rise to suitable band gap, lower recombination rate of charge carriers, larger specific surface area and increased light absorption. Meanwhile, when the amount of WO_x-EDA exceeds 40 wt%, the photocatalytic capability decreases gradually which could be attributed to the poor catalytic performance of WO_3. It is well known that the dye sensitization could contribute to dye degradation and we choose a colorless pollutant phenol to evaluate the performance of WO_3/g-C_3N_4 photocatalysts in order to exclude the dye sensitization effect. According to Fig. S7,† all samples show the degradation of phenol and WO_3/g-C_3N_4 composites show higher photocatalytic performance than pure g-C_3N_4 and WO_3. The above phenol degradation results, which are consistent with RhB degradation, well exclude the disturbing of dye sensitization.

To demonstrate the advantages of WO_x-EDA precursor, commercial WO_3 (bought from Aladdin) was selected instead of WO_x-EDA as precursor to prepare WO_3/g-C_3N_4 composites. According to different mass ratio between commercial WO_3 and CN, the samples were named CN, WCN20, WCN40, WCN60, WCN80, and WO_3(C). The above samples were prepared by the same process according to the g-C_3N_4 nanosheets loading with WO_3 nanoparticles using WO_x-EDA as precursor and its photocatalytic performance was tested with the same conditions under visible light illumination (Fig. S8†). Among the above six samples, WCN60 shows the highest photocatalytic activity with the 68% degradation of RhB after 30 min visible light irradiation, but it is still lower than WECN20 (89%) which was prepared using WO_3-EDA nanobelts as precursor. The poor photocatalytic performance could be attributed to its large particles size of commercial WO_3, which can be seen in Fig. S7.†

Recycling tests of the WO_3/g-C_3N_4 composites are carried out to assess photostability and recyclability as shown in Fig. 7(d). The degradation of RhB for WECN40 sample, from 89% to 85% in the first and sixth cycle respectively, remains relative stable without distinct fluctuation throughout six runs under visible light irradiation. Furthermore, the main diffraction peaks of XRD of the catalyst, before and after reaction, retain almost the same which implies the structural stability. Only the 2θ at around 31° may ascribe to catalyst contamination or reaction between sample and aqueous solution. The stability of photocatalytic performance and crystal phase implies the interaction between g-C_3N_4 and WO_3 is relative strong.

Electrochemical characterization

To further support the restrained recombination of photo-induced electron–hole pairs for the WO_3/g-C_3N_4 composites, the transient photocurrent response tests were carried out for several on–off cycles under visible light irradiation (Fig. S9†). The WECN40 exhibits higher photocurrent intensity than that of CN, which is in accordance with its enhanced photocatalytic degradation rate under visible light irradiation. The fact indicates that the WO_3/g-C_3N_4 composites show better separation or transfer of photo-induced electrons and holes, which is also in accordance with the PL spectra results. For WO_3 sample, it holds high photocurrent intensity, nevertheless, the inappropriate CB position limits its photocatalytic activity under visible light illumination.[24,25]

Possible photocatalytic mechanism

To investigate the photocatalytic mechanism of the WO_3/g-C_3N_4 composites, several scavengers were applied to check the active species during the photodegradation process under visible light irradiation (Fig. 8). Ethylenediaminetetraacetic acid disodium salt (EDTA-2Na), *tert* butyl alcohol (TBA) and 1,4-benzoquinone (BQ) were employed as the hole (h^+) scavenger, hydroxyl radical ($^{\bullet}OH$) scavenger and superoxide radical ($^{\bullet}O_2^-$) scavenger. It is clear that the degradation of organic pollutants decreases by the addition of scavengers compared with catalyst without any

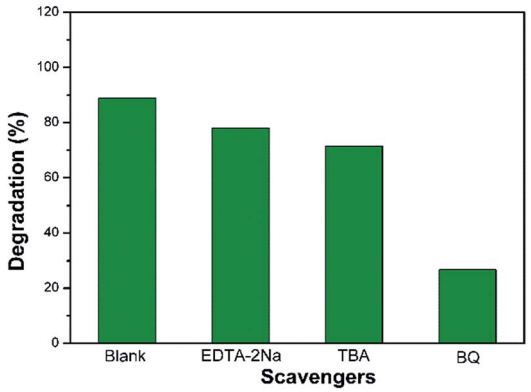

Fig. 8 The effects of various scavengers on the photodegradation of WO_3/g-C_3N_4 composite (WECN40) under visible light.

scavengers, implying that reactive species are significant for the RhB degradation in aqueous solution under visible light. What's more, the effect of the scavengers of TBA and BQ based on suppression of RhB degradation is much bigger than that of EDTA-2Na, indicating that the species of hydroxyl radical ($^{\bullet}OH$) and superoxide radical ($^{\bullet}O_2^-$) are the major active species in this photocatalytic system.

Based on the above analysis, a proposed mechanism for the improved photocatalytic activity is briefly described in Fig. 9. For g-C_3N_4, the CB and VB potentials are 1.62 and −1.09 eV respectively, whereas these values of WO_3 are 2.70 and −0.17 eV respectively. The g-C_3N_4 and WO_3 would be excited and the transition of electrons from VB to CB will happen in both semiconductor under visible light irradiation. Because the VB level of g-C_3N_4 is more negative than that of WO_3 and the CB potential of WO_3 is more positive than that of g-C_3N_4, the photo-generated holes can transfer from the VB of WO_3 to that of g-C_3N_4. Meanwhile, the photo-excited electrons in the CB of g-C_3N_4 could move to the CB of WO_3. These electrons can react with W^{6+} species in the WO_3 and then W^{6+} be reduced into W^{5+}. The W^{5+} ions in the surface of WO_3 can be re-oxidized into W^{6+} through the reaction with oxygen to generate superoxide radical ($^{\bullet}O_2^-$). Superoxide radical ($^{\bullet}O_2^-$) can also react with H_2O molecules to form $^{\bullet}OH$.[30] Hydroxyl radical ($^{\bullet}OH$) and superoxide radical ($^{\bullet}O_2^-$) are the main species to degrade RhB into CO_2 and H_2O under visible light irradiation. Hence, it is concluded that g-C_3N_4 coupling with WO_3 increases the separation efficiency of the photo-induced holes and electrons through reduction or oxidation reaction in the surface of composites under visible light illumination.

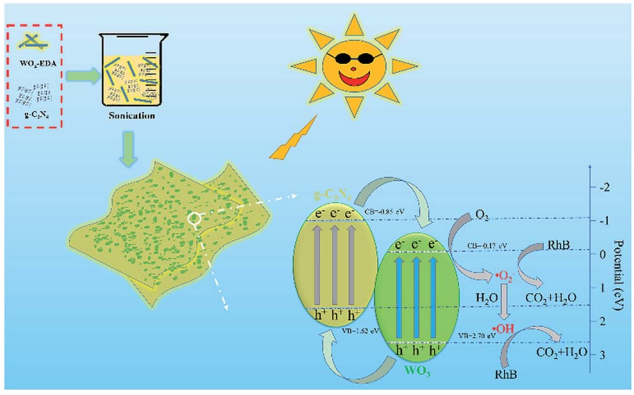

Fig. 9 Possible degradation mechanism of RhB for photocatalysts under visible light illumination.

Conclusions

The WO_3/g-C_3N_4 composites were facile prepared through heat treatment of WO_x-EDA nanobelts and g-C_3N_4 powder. The heat treatment temperature of 400 °C is the key factor to obtain g-C_3N_4 nanosheets with uniformly dispersed WO_3 nanoparticles. The enhanced photocatalytic performance is considered to arise from the increased reaction sites, enhanced visible light absorption and the restrained recombination of photo-induced electron–hole pairs under visible light irradiation. The WO_3/g-C_3N_4 composite exhibits best activity for the degradation of RhB when the amount of WO_x-EDA reached 40 wt% in the mixture with g-C_3N_4. Meanwhile, it is concluded that the species of hydroxyl radical ($^{\bullet}OH$) and superoxide radical ($^{\bullet}O_2^-$) are the major active species in the photocatalytic system. Therefore, this work demonstrates a method using WO_x-EDA as precursor, which could improve the photocatalytic degradation under visible light illumination. And it also provides the reference for other composites synthesis.

Acknowledgements

This work was supported by National Nature Science Foundation of China (grant number: 11234011, 11327901, 51102208), the Fundamental Research Funds for the Central Universities (2014QNA4008).

Notes and references

1 A. Houas, H. Lachheb, M. Ksibi, E. Elaloui, C. Guillard and J. M. Herrmann, *Appl. Catal., B*, 2001, **31**, 145–157.
2 W. Ren, Z. Ai, F. Jia, L. Zhang, X. Fan and Z. Zou, *Appl. Catal., B*, 2007, **69**, 138–144.
3 M. Ge, C. Cao, J. Huang, S. Li, Z. Chen, K. Q. Zhang, S. S. Al Deyab and Y. Lai, *J. Mater. Chem. A*, 2016, **4**, 6772–6801.
4 O. Ola and M. M. Maroto-Valer, *J. Photochem. Photobiol., C*, 2015, **24**, 16–42.
5 K. Maeda and K. Domen, *J. Phys. Chem. Lett.*, 2010, **1**, 2655–2661.
6 H. Tong, S. Ouyang, Y. Bi, N. Umezawa, M. Oshikiri and J. Ye, *Adv. Mater.*, 2012, **24**, 229–251.
7 X. Wang, K. Maeda, A. Thomas, K. Takanabe, G. Xin, J. M. Carlsson, K. Domen and M. Antonietti, *Nat. Mater.*, 2009, **8**, 76–80.
8 Z. Zhao, Y. Sun and F. Dong, *Nanoscale*, 2015, **7**, 15–37.
9 S. Cao, J. Low, J. Yu and M. Jaroniec, *Adv. Mater.*, 2015, **27**, 2150–2176.
10 S. W. Cao, X. F. Liu, Y. P. Yuan, Z. Y. Zhang, J. Fang, S. C. Loo, J. Barber, T. C. Sum and C. Xue, *Phys. Chem. Chem. Phys.*, 2013, **15**, 18363–18366.

11 F. Raziq, Y. Qu, X. Zhang, M. Humayun, J. Wu, A. Zada, H. Yu, X. Sun and L. Jing, *J. Phys. Chem. C*, 2016, **120**, 98–107.
12 J. Fu, Y. Tian, B. Chang, F. Xi and X. Dong, *J. Mater. Chem.*, 2012, **22**, 21159–21166.
13 F. Dong, L. Wu, Y. Sun, M. Fu, Z. Wu and S. C. Lee, *J. Mater. Chem.*, 2011, **21**, 15171–15174.
14 K. Dai, L. Lu, C. Liang, Q. Liu and G. Zhu, *Appl. Catal., B*, 2014, **156–157**, 331–340.
15 K. Dai, L. Lu, Q. Liu, G. Zhu, X. Wei, J. Bai, L. Xuan and H. Wang, *Dalton Trans.*, 2014, **43**, 6295–6299.
16 P. Niu, L. Zhang, G. Liu and H.-M. Cheng, *Adv. Funct. Mater.*, 2012, **22**, 4763–4770.
17 T. Sano, S. Tsutsui, K. Koike, T. Hirakawa, Y. Teramoto, N. Negishi and K. Takeuchi, *J. Mater. Chem. A*, 2013, **1**, 479–485.
18 S. C. Yan, Z. S. Li and Z. G. Zou, *Langmuir*, 2010, **26**, 3894–3901.
19 L. Ge, C. Han, J. Liu and Y. Li, *Appl. Catal., A*, 2011, **409–410**, 215–222.
20 W. Jiang, W. Luo, J. Wang, M. Zhang and Y. Zhu, *J. Photochem. Photobiol., C*, 2016, **28**, 87–115.
21 X. Dong and F. Cheng, *J. Mater. Chem. A*, 2015, **3**, 23642–23652.
22 G. Mamba and A. K. Mishra, *Appl. Catal., B*, 2016, **198**, 347–377.
23 L. Shen, Z. Xing, J. Zou, Z. Li, X. Wu, Y. Zhang, Q. Zhu, S. Yang and W. Zhou, *Sci. Rep.*, 2017, **7**, 41978–41989.
24 X. Yuan, C. Zhou, Q. Jing, Q. Tang, Y. Mu and A. K. Du, *Nanomaterials*, 2016, **6**, 173–185.
25 F. Chen, D. Li, B. Luo, M. Chen and W. Shi, *J. Alloys Compd.*, 2017, **694**, 193–200.
26 Y. Cao, Q. Li and W. Wang, *RSC Adv.*, 2017, **7**, 6131–6139.
27 H. Reiche, W. W. Dunn and A. J. Bard, *J. Phys. Chem.*, 1979, **83**, 2248–2251.
28 S. G. Kumar and K. S. R. K. Rao, *Appl. Surf. Sci.*, 2015, **355**, 939–958.
29 S. Chen, Y. Hu, S. Meng and X. Fu, *Appl. Catal., B*, 2014, **150–151**, 564–573.
30 I. Aslam, C. Cao, M. Tanveer, W. S. Khan, M. Tahir, M. Abid, F. Idrees, F. K. Butt, Z. Ali and N. Mahmood, *New J. Chem.*, 2014, **38**, 5462–5469.
31 M. A. Gondal, A. A. Adesida, S. G. Rashid, S. Shi, R. Khan, Z. H. Yamani, K. Shen, Q. Xu, Z. S. Seddigi and X. Chang, *React. Kinet., Mech. Catal.*, 2014, **114**, 357–367.
32 H. Katsumata, Y. Tachi, T. Suzuki and S. Kaneco, *RSC Adv.*, 2014, **4**, 21405–21409.
33 J. Ding, Q. Liu, Z. Zhang, X. Liu, J. Zhao, S. Cheng, B. Zong and W. L. Dai, *Appl. Catal., B*, 2015, **165**, 511–518.
34 X. Hu, Q. Ji, J. P. Hill and K. Ariga, *CrystEngComm*, 2011, **13**, 2237–2241.
35 S. C. Yan, Z. S. Li and Z. G. Zou, *Langmuir*, 2009, **25**, 10397–10401.
36 L. Ye, J. Liu, Z. Jiang, T. Peng and L. Zan, *Appl. Catal., B*, 2013, **142–143**, 1–7.
37 R. Wu, J. Zhang, Y. Shi, D. Liu and B. Zhang, *J. Am. Chem. Soc.*, 2015, **137**, 6983–6986.
38 V. N. Khabashesku, J. L. Zimmerman and J. L. Margrave, *Chem. Mater.*, 2000, **12**, 3264–3270.
39 J. L. Zimmerman, R. Williams, V. N. Khabashesku and J. L. Margrave, *Nano Lett.*, 2001, **1**, 731–734.
40 Y. J. Bai, B. Lü, Z. G. Liu, L. Li, D.-L. Cui, X. G. Xu and Q. L. Wang, *J. Cryst. Growth*, 2003, **247**, 505–508.
41 J. H. Kaufman, S. Metin and D. D. Saperstein, *Phys. Rev. B: Condens. Matter Mater. Phys.*, 1989, **39**, 13053–13060.
42 A. Bousetta, M. Lu, A. Bensaoula and A. Schultz, *Appl. Phys. Lett.*, 1994, **65**, 696–698.
43 Q. Fu, C. B. Cao and H. S. Zhu, *Chem. Phys. Lett.*, 1999, **314**, 223–226.
44 H.-X. Han and B. J. Feldman, *Solid State Commun.*, 1988, **65**, 921–923.
45 Z. A. Huang, Q. Sun, K. Lv, Z. Zhang, M. Li and B. Li, *Appl. Catal., B*, 2015, **164**, 420–427.
46 R. J. Colton and J. W. Rabalais, *Inorg. Chem.*, 1976, **15**, 236–238.
47 M. Sun, N. Xu, Y. Cao, J. Yao and E. Wang, *J. Mater. Res.*, 2000, **15**, 927–933.
48 M. Feng, A. L. Pan, H. R. Zhang, Z. A. Li, F. Liu, H. W. Liu, D. X. Shi, B. S. Zou and H. J. Gao, *Appl. Phys. Lett.*, 2005, **86**, 141901–141903.
49 Y. Liu, S. Xie, C. Liu, J. Li, X. Lu and Y. Tong, *J. Power Sources*, 2014, **269**, 98–103.
50 G. Zhang, J. Zhang, M. Zhang and X. Wang, *J. Mater. Chem.*, 2012, **22**, 8525–8531.
51 A. Vinu, K. Ariga, T. Mori, T. Nakanishi, S. Hishita, D. Golberg and Y. Bando, *Adv. Mater.*, 2005, **17**, 1648–1652.
52 H. Katsumata, T. Sakai, T. Suzuki and S. Kaneco, *Ind. Eng. Chem. Res.*, 2014, **53**, 8018–8025.
53 H. Zhang, J. Yang, D. Li, W. Guo, Q. Qin, L. Zhu and W. Zheng, *Appl. Surf. Sci.*, 2014, **305**, 274–280.
54 H. Song, Y. Li, Z. Lou, M. Xiao, L. Hu, Z. Ye and L. Zhu, *Appl. Catal., B*, 2015, **166–167**, 112–120.
55 C. Bi, J. Cao, H. Lina, Y. Wang and S. Chen, *Appl. Catal., B*, 2016, **195**, 132–140.
56 Q. Xiang, J. Yu and M. Jaroniec, *J. Phys. Chem. C*, 2011, **115**, 7355–7363.
57 J.-H. Ha, P. Muralidharan and D. K. Kim, *J. Alloys Compd.*, 2009, **475**, 446–451.
58 H. Fu, C. Pan, W. Yao and Y. Zhu, *J. Phys. Chem. B*, 2005, **109**, 22432–22439.
59 K. Hayat, M. A. Gondal, M. M. Khaled, S. Ahmed and A. M. Shemsi, *Appl. Catal., A*, 2011, **393**, 122–129.

